



Study of the spectroscopic, magnetic, and electrical behavior of PVDF/PEO blend incorporated with nickel ferrite (NiFe_2O_4) nanoparticles

I. S. Elashmawi¹ · A. M. Ismail¹

Received: 20 November 2021 / Revised: 5 February 2022 / Accepted: 9 February 2022 /

Published online: 9 March 2022

© The Author(s) 2022

Abstract

Pure nickel ferrite nanoparticles (NiFe_2O_4 NPs) were prepared by the solvothermal method. Different concentrations of NiFe_2O_4 were added to PVDF/PEO blend to prepare the PVDF/PEO- NiFe_2O_4 nanocomposite films. The films were characterized using different techniques in detail. Pure NiFe_2O_4 NPs images have a semispherical shape and roundness of the edges, with average particle size ~ 4.3 – 8.8 nm, and polycrystalline structure. Pure NiFe_2O_4 NPs show that micrometrical agglomeration suggests the presence of pore-free crystallites on the surface. The spectroscopic techniques such as XRD, FTIR, and UV–visible have confirmed the interaction between PVDF/PEO and NiFe_2O_4 NPs. Still, the nanocomposites exhibit a smooth surface with typical spherulitic clusters revealing the semi-crystalline structure of the PVDF/PEO- NiFe_2O_4 nanocomposites. The values of ϵ' and ϵ'' were increased as an increase of NiFe_2O_4 due to the high value of dielectric permittivity of NiFe_2O_4 . The appearance of semi-circles in the plot of M'' with Log confirms the single phase of the samples. The dielectric measurements show that M' is inversely proportional to ϵ' . At higher temperatures, M' levels off at frequencies higher than those at lower temperatures because the relaxation processes were spread over a range of frequencies. The values of saturation magnetization of PVDF/PEO- NiFe_2O_4 films were linearly increased as an increase of NiFe_2O_4 indicates improvement in the magnetic vector arrangement. Due to the enhancement of the magnetic properties, they can further exploit the films for magnetic applications.

Keywords NiFe_2O_4 NPs · PVDF/PEO- NiFe_2O_4 nanocomposites · XRD · AT-IR · VSM measurement

✉ I. S. Elashmawi
islam_shukri2000@yahoo.com

¹ Spectroscopy Department; Physics Research Institute, National Research Centre, Dokki, Giza 12622, Egypt

Introduction

In the past years, the science of polymeric nanocomposites has demonstrated its potential in many applications in the electronics and technology fields. Therefore, ferrites and magnetic nanomaterials with appropriate physical and chemical properties that contain transition elements (XFe_2O_4) (where $X = Mn, Mg, Co, Fe, Ni$ or Zn). The magnetic ferrites are used for diagnostic purposes, computer memory storage and drug guidance. This is due to its impressive size and shape-dependent magnetic properties. Nickel ferrite ($NiFe_2O_4$) has many applications for its high magnetic anisotropy, high saturation magnetization, and supermagnetic structure. $NiFe_2O_4$ has a wide range of magnetic properties based on particle size and morphology, such as super magnetic behavior [1–11].

Researchers have recently been interested in nanotechnology, especially nanocrystalline materials [12, 13], which play a general role in many applications due to their unique electrical and magnetic properties, such as storing magnetic information with a high density. Nickel ferrite ($NiFe_2O_4$) is a versatile soft ferrite material that is technological of great importance for its ideal magnetic properties such as gas sensor, magnetic storage systems, magneto-optical, magneto resistive, magnetic resonance imaging and microwave devices. $NiFe_2O_4$ has a cubic structure with an inverse spinel structure and shows suitable ferromagnetism arising from magnetic moment of antiparallel rotation [14, 15]. Spinel nickel ferrite ($NiFe_2O_4$) [16], among the most significant ferrite materials, has been extensively researched due to its wide range of applications, including catalysts, magnetic materials, microwave devices, gas sensors [17]. $NiFe_2O_4$ has an inverse spinel structure and has a cubic structure [18].

Polymer nanocomposites are one of new nanocomposites in which the polymer acts as the matrices with other nanoscale components such as the nanofiller [19, 20]. Various inorganic fillers have been added to the polymeric matrices to improve their properties [21]. Poly ethylene oxide (PEO) has become the most investigated as a promising polymer. PEO is a soluble in water, highly crystalline thermoplastic with a moderate tensile modulus, good mechanical and electrical characteristics [22]. The high crystallinity of PEO is detrimental to their ionic conductivity. The PEO-based electrolytes have been found to have low ionic conductivity in the range of temperatures [23]. The suggestion for mixing PEO could solve the brittleness problem while also improving the system's ionic conductivity [24]. Polyvinylidene fluoride (PVDF) is a highly concentrated polymeric material. Pyroelectric and piezoelectric capabilities have been observed. PVDF and its mixes (with one or more other polymers) have gotten a lot of press in recent years for advanced techniques [22]. PVDF with fillers or nanofillers is widely used for improved performance and extended uses [25].

In our paper, $NiFe_2O_4$ nanoparticles are prepared using the solvothermal method and are characterized using XRD, TEM, FESEM and ATR-FTIR techniques. Then, studying for the first one, their addition on (85/15 wt/wt%) PVDF/PEO using casting technique methods to be used in industrial application and

characterized using XRD, FESEM, ATR-FTIR, magnetic properties and also the dielectric properties are studied.

Experimental work

Material

Ferric nitrate nonahydrate ($\text{Fe}(\text{NO}_3)_3 \cdot 9\text{H}_2\text{O}$), LobaChemie PVT. LTD. With purity of 98%. Nickel (II) nitrate hexahydrate ($\text{Ni}(\text{NO}_3)_2 \cdot 6\text{H}_2\text{O}$), Sigma-Aldrich, USA. Ammonium hydroxide solution (NH_4OH), AbcoChemie, England, assay 28–30% NH_3 (AR). Ethylene glycol, Sigma-Aldrich, USA. Alfa Aesar provided PVDF with an M.W. of 572,000, and ACROS provided PEO (99.9%) with an M.W. of 600,000. SD Fine Chemicals supplied the dimethyl sulfoxide (DMSO).

Preparation of NiFe_2O_4 nanoparticles

The molar ratio (2:1) of $\text{Fe}(\text{NO}_3)_3 \cdot 9\text{H}_2\text{O}$ and $\text{Ni}(\text{NO}_3)_2 \cdot 6\text{H}_2\text{O}$ were dissolved in 75 mL ethylene. Then, at pH 12, added NH_4OH solution. The mixture was then placed in the autoclave and heated in an oven about 72 hat 200 °C to complete the chemical reaction procedures and form NiFe_2O_4 nanoparticles. The chemical residue (NiFe_2O_4 nanoparticles) was washed multiple times with ethanol and distilled water before being dried at 70 °C. The NiFe_2O_4 nanoparticles were obtained.

Preparation of PVDF/PEO- NiFe_2O_4 nanocomposites

Amount (85/15 wt/wt%) of PVDF/PEO was dissolved in dimethyl sulfoxide (DMSO) as a filler with regularly stirred until uniform viscous liquid. Drop by drop, the produced NiFe_2O_4 NPs in mass fractions of 2, 4, 6, 8 and 10 wt% was added to the PVDF/PEO solution. The resultant solution was sonicated to achieve homogeneity and a good dispersed solution. The solution was then cast onto Petri dishes and stored for 12 h in a vacuum oven at 70 °C until the solvent had completely evaporated.

Measurement techniques

Determined the crystallinity of the prepared films from X-ray diffraction (XRD) spectra, which were captured using a PANalyticalX'Pert Pro diffractometer with Cu- K radiation in the 2θ range from 5° to 60°. Transmission electron microscope (TEM) (JEM-2100F electron microscope) at 200 kV was used to determine the size of NiFe_2O_4 NPs. A field emission scanning electron microscope (FESEM) (Quanta 250 FEG) was used to examine the morphology of the samples (EDS). Using Gwyddion software, 3D micrographs and roughness were characteristics from FESEM picture. The comparative examination of the films was analyzed using Vertex 80 Bruker in attenuated total reflectance (ATR) mode

in the wavenumber from 2000 to 400 cm^{-1} . UV–Vis spectra were obtained at room temperature with a Jasco V-630 spectrophotometer about 200–1000 nm. The magnetic properties of the samples were carried out at room temperature in the range from $-20,000$ to $+20,000$ Oe using a vibrating sample magnetometer (VSM) (AGM & VSM Magnetometer, MicroMag 3900 series from former Princeton Measurement Co., currently Lake Shore Cryotronics, Inc., Westerville, OH, USA). A high-resolution Alpha-A Analyzer from Novocontrol was used to make broadband dielectric spectroscopic measurements in the frequency range 0.1 Hz to 7 MHz.

Results and discussion

Figure 1a–d represents XRD, TEM, histogram, and SAED of the prepared pure NiFe_2O_4 nanoparticles. As seen from XRD, there are sharp crystalline peaks at $2\theta = 18.3^\circ$, 30.6° , 35.8° and 57.3° , which corresponds to (111), (220), (311), (400) and (511) miller index, respectively, which agree with JCPDS Card No.

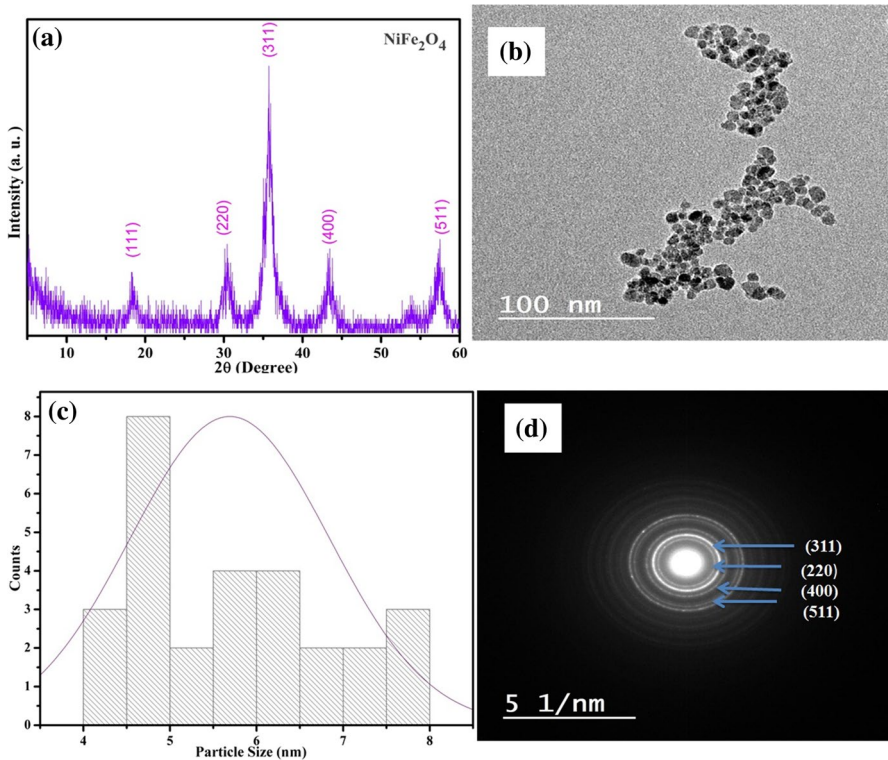


Fig. 1 a The XRD, b HRTEM, c Histogram and d SAED of the prepared NiFe_2O_4 NPs

10-032. There are not any impurity peaks found, which confirmed the high purity of the prepared NiFe₂O₄. The average crystal size (*S*) of pure NiFe₂O₄ is estimated using Scherrer equation [26]:

$$S = \frac{0.89\lambda}{\mu \cos \theta} \tag{1}$$

where λ is the X-ray wavelength (1.5408 Å), μ is defined as the full width at half maximum peak and θ (rad) is the Bragg angle. The calculated average crystal size of pure NiFe₂O₄ nanoparticles is found to be 5.3 nm.

As stated in the formula below, values of lattice constant (*a*) were obtained using information from the ‘Miller indices (*h k l*)’ and inter-planar spacing (*d*) values [27]:

$$a = d\sqrt{h^2 + k^2 + l^2} \tag{2}$$

The inter-planar spacing *d* of the most intense peak (311) is given from the below equation [28]:

$$d = \frac{\lambda}{2 \sin \theta} \tag{3}$$

The calculated lattice constant of the most intense peak (311) is 8.29 Å. The following relation was used to calculate the unit cell volume of NiFe₂O₄ NPs which is proportional to the lattice constant values [29]:

$$V = a^3 \tag{4}$$

The unit cell volume is 569.72 Å³. The dislocation density (δ) was calculated using the equation below using the average crystallite size values and it is found to be equal 3.5 × 10¹⁶ lines/m²:

$$\delta = 1/S^2 \tag{5}$$

The following equations were used to calculate the hopping length (*L_A* and *L_B*) values [30, 31]:

$$L_A = a\sqrt{\frac{3}{4}} \quad \text{and} \quad L_B = a\sqrt{\frac{2}{4}} \tag{6}$$

Values of *L_A* and *L_B* are 7.17 Å and 5.86 Å.

The TEM of pure NiFe₂O₄ NPs has a semispherical shape with the roundness of some edges with an average particle size of nearly 4.3–8.8 nm calculated from the histogram. The result agrees with XRD data computed using Scherrer’s formula. Let us get the concept of a lattice and how atoms are arranged basically. So advanced specific area electron diffraction (SAED) spectrum is a two-dimensional spectrum obtained in a reciprocal lattice. SAED gives us a more accurate idea of the crystal structure. The SAED study shows a superimposed bright ring-shaped spot around the center point with varying diameters confirming the polycrystalline structure of pure NiFe₂O₄ material.

Figure 2 shows XRD diffraction of (85/15 wt/wt%) PVDF/PEO and PVDF/PEO doped with the different weight percentages (2, 4, 6, 8 and 10 wt) of NiFe_2O_4 NPs. As seen for undoped PVDF/PEO, there are diffraction patterns at $2\theta=18.7^\circ$, 20.2° , 36.2° and 39.4° [32, 33]. For PVDF/PEO modified with NiFe_2O_4 NPs, the diffraction pattern at $2\theta=20.2^\circ$ shifted toward a higher theta degree and their broadening increased with NiFe_2O_4 NPs. Also, there is a noticeable decrease in their intensity compared to the undoped blend. Besides, the diffraction peaks at $2\theta=18.7^\circ$ and 39.4° are disappeared with the increase of NiFe_2O_4 NPs, confirming the interaction between PVDF/PEO and the prepared NiFe_2O_4 NPs. Scheme 1 represents the possible chemical reaction between PVDF/PEO and NiFe_2O_4 NPs.

The morphological study and energy-dispersive X-ray (EDX) analysis of the prepared NiFe_2O_4 NPs is shown in Fig. 3. The samples have a micrometrical agglomeration of small particles, as shown in the FESEM image. The presence of high-density accumulation suggests the presence of pore-free crystallites on the surface. The nanoparticles agglomerate and develop into larger assemblies due to their high surface energy. The EDX analysis confirmed the formation of NiFe_2O_4 NPs within the presence of the basic component NiFe_2O_4 NPs and affirmed the high purity of the prepared nanoparticles.

Figure 4a–c shows FESEM images of PVDF/PEO, PVDF/PEO/4 wt% NiFe_2O_4 NPs and PVDF/PEO-10 wt% NiFe_2O_4 NPs. Figure 4a exhibits a smooth surface with typical spherulitic clusters, reveals the semi-crystalline structure of PEO [34].

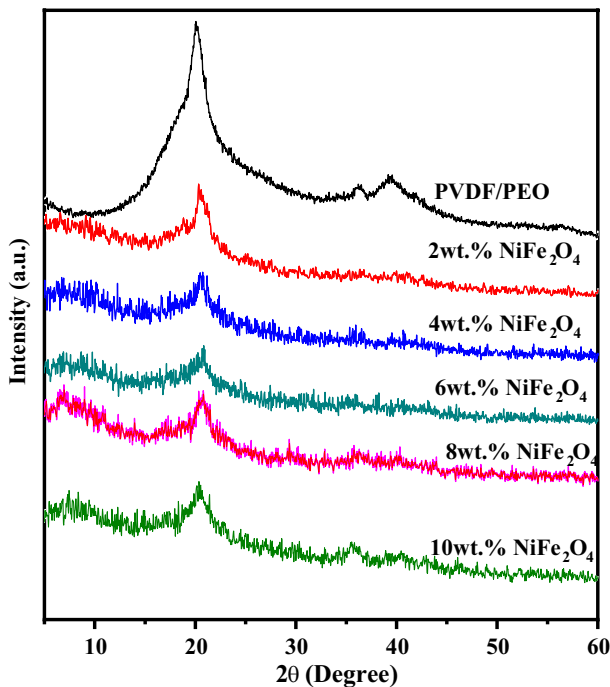
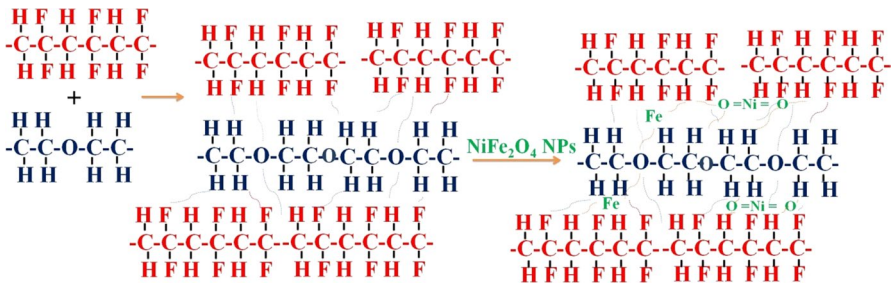


Fig. 2 XRD of (85/15 wt/wt%) PVDF/PEO and PVDF/PEO incorporated with (2, 4, 6, 8, 10 wt%) NiFe_2O_4 NPs



Scheme 1 The possible chemical reactions between PVDF/PEO and NiFe_2O_4 NPs

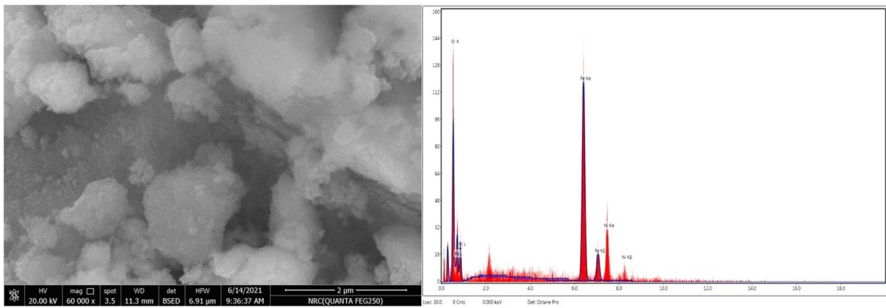


Fig. 3 FESEM and EDX analysis of NiFe_2O_4 NPs

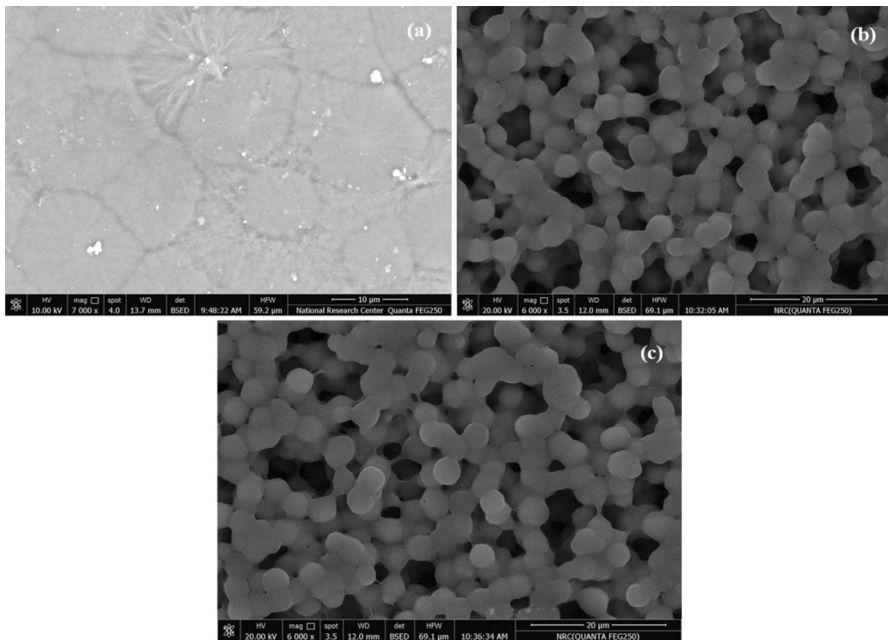


Fig. 4 SEM images of **a** (85/15 wt/wt%) PVDF/PEO and PVDF/PEO incorporated with **b** 4 wt% NiFe_2O_4 NPs and **c** 10 wt% NiFe_2O_4 NPs

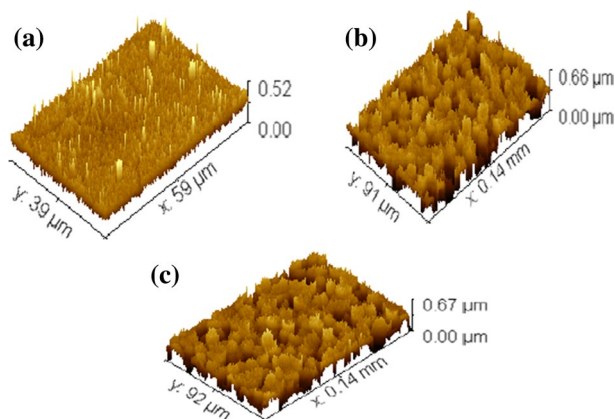


Fig. 5 3D images of **a** (85/15 wt/wt%) PVDF/PEO and PVDF/PEO incorporated with **b** 4 wt% NiFe₂O₄ NPs and **c** 10 wt% NiFe₂O₄ NPs

Table 1 Roughness average (R_a), root mean square roughness (R_q), maximum height of roughness (R_T) of PVDF/PEO and PVDF/PEO-4 and PVDF/PEO-10 wt% of NiFe₂O₄ NPs

| Sample | R_a (nm) | R_q (nm) | R_T (nm) |
|--|------------|------------|------------|
| PVDF/PEO | 0.25 | 0.05 | 0.26 |
| PVDF/PEO-4 wt% NiFe ₂ O ₄ | 279.4 | 108.7 | 379.4 |
| PVDF/PEO-10 wt% NiFe ₂ O ₄ | 274.3 | 107.7 | 396.3 |

As shown in Fig. 4b, there is no visible interface between the 2 polymers, indicating that PVDF and PEO are compatible. Figure 4b, c depicts a homogenous multiferoic sphere fabrication with good dispersion and spherical form. The sizes of the spheres ranged from 3 to 5 μm , which means that NiFe₂O₄ NPs magnetic fillers are inserted into the PVDF/PEO polymer chains. Figure 5 shows 3D images of (85/15 wt/wt%) PVDF/PEO and PVDF/PEO incorporated with 4 wt % NiFe₂O₄ NPs and 10 wt% NiFe₂O₄ NPs. The 3D image reveals that polymer nanocomposite's surface becomes rougher (see Table 1) compared to pure polymer blend which means that the PVDF/PEO-NiFe₂O₄ NPs improve the polymer blend surface to be suitable to apply in many industrial applications.

Figure 6 represents ATR-FTIR of NiFe₂O₄ NPs, (85/15 wt/wt%) PVDF/PEO and PVDF/PEO incorporated with (2, 4, 6, 8 and 10 wt%) NiFe₂O₄ NPs. As seen for NiFe₂O₄ NPs, the symmetric and asymmetric –OH stretching caused by adsorbed water is shown by an absorption band at 3247 cm^{-1} . The –OH stretching is also represented by the peak at 2932 cm^{-1} coupled with 2864 cm^{-1} . Bands at 1648 cm^{-1} and 1385 cm^{-1} correspond to the –OH bending of absorbed hydrates. The Fe–O and Ni–O stretching modes are present at 574 cm^{-1} and 422 cm^{-1} , indicating the creation of NiFe₂O₄ NPs [18, 35]. For (85/15 wt/wt%) PVDF/PEO, according to previous literature [18, 36, 37], band at 1400 cm^{-1} corresponds to wagging modes of CH₂, 1231 cm^{-1} attributed to CH₂ twisting mode of PEO. The band at 1170 cm^{-1} is due to the stretching mode of CF₂ of PVDF. The band at 1071 cm^{-1} corresponded to the stretching mode of C–O of PEO.

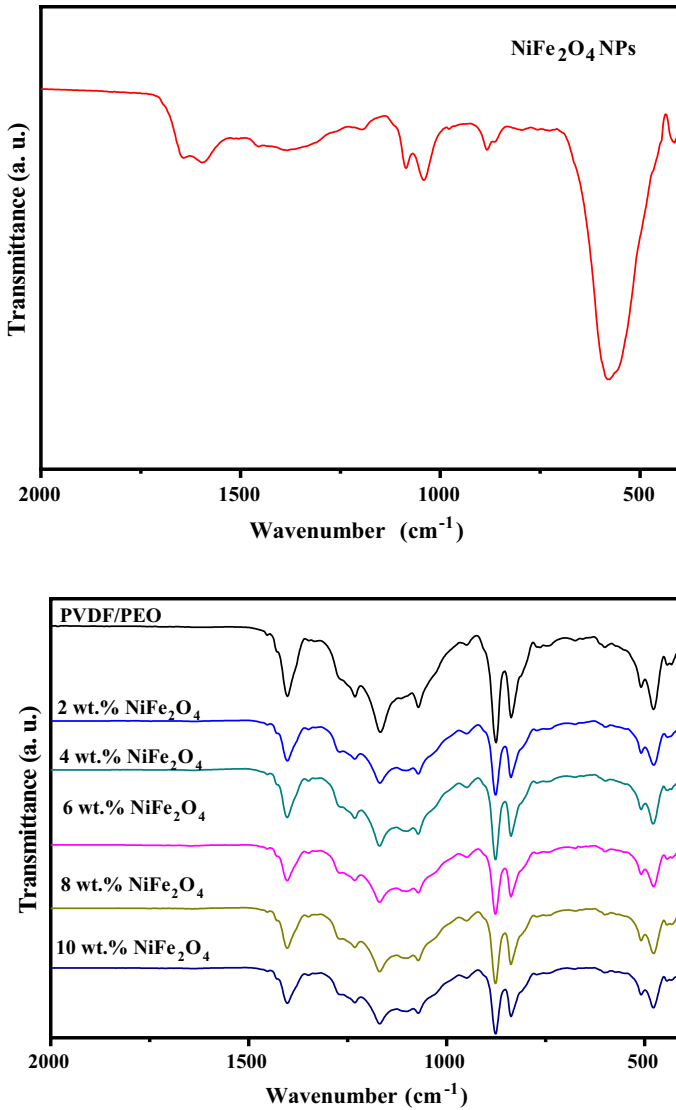


Fig. 6 ATR-FTIR of NiFe₂O₄ NPs, (85/15 wt/wt%) PVDF/PEO and PVDF/PEO incorporated with (2, 4, 6, 8, 10 wt%) NiFe₂O₄ NPs

Bands at 874 cm⁻¹ and 835 cm⁻¹ correspond to the vibration of C–O and CH₂ rocking mode of PVDF/PEO. The bending vibration of C–F₂ is seen at 675 cm⁻¹ and 477 cm⁻¹. The bending and wagging vibrations of CF₂ are attributed to the vibrational peaks at 500 cm⁻¹ and 416 cm⁻¹, respectively.

For PVDF/PEO doped with (2, 4, 6, 8 and 10 wt %) NiFe₂O₄ NPs, a new band appears at 1109 cm⁻¹ and the band at 675 cm⁻¹ is nearly disappeared with the addition of NiFe₂O₄ NPs. Also, there is a noticeable decrease in the intensities of

all bands with the addition of NiFe₂O₄ NPs. All the above results confirmed the miscibility and complexation between PVDF/PEO and NiFe₂O₄ NPs.

Figure 7 represents UV–Vis spectra of 85/15 wt/wt% of PVDF/PEO and PVDF/PEO incorporated with (2, 4, 6, 8 and 10 wt%) NiFe₂O₄ NPs. As seen for pure PVDF/PEO blend, an absorption peak at 192 nm is assigned to π – π^* (chromophoric group of PVDF/PEO) [37]. An increase of NiFe₂O₄, this peak shifts toward a higher wavelength with the broadening of the peak. Another peak appeared at 348 nm [38], which was assigned to NiFe₂O₄ NPs. The intensity of this peak is gradually increased with increases of NiFe₂O₄ NPs. The data suggested that the interaction between NiFe₂O₄ NPs and PVDF/PEO occurs.

The dielectric behavior of the material has been studied over a wide range of frequencies from 0.1 Hz to 7 MHz and temperatures from 30 to 120 °C. The complex impedance spectroscopy technique enables us to separate the real (ϵ') and imaginary (ϵ'') components of the dielectric parameters and hence provides a true picture of the properties of materials. The dielectric permittivity (ϵ^*) is expressed as [39, 40]:

$$\epsilon^* = \epsilon' - i\epsilon'' \quad (7)$$

The variation between ϵ' and ϵ'' with Log (f) for PVDF/PEO blend doped by 0, 2, 4, 6, 8 and 10 wt% of nickel ferrite (NiFe₂O₄) in the range of frequency about 0.1 Hz to 7 GHz at room temperature is shown in Fig. 8a, b. The figures display that the dielectric constant (ϵ') dramatically decreases with an increase in frequency. At low frequencies, dipoles follow the field. The values of dielectric constant (ϵ') are very high due to 2 sources, one of them associated with mobile carriers and the other because the studied material is polarized in structure. As the frequency increases, dipoles begin to lag behind the field, so the dielectric constant decreases. When frequency reaches the characteristic frequency, the

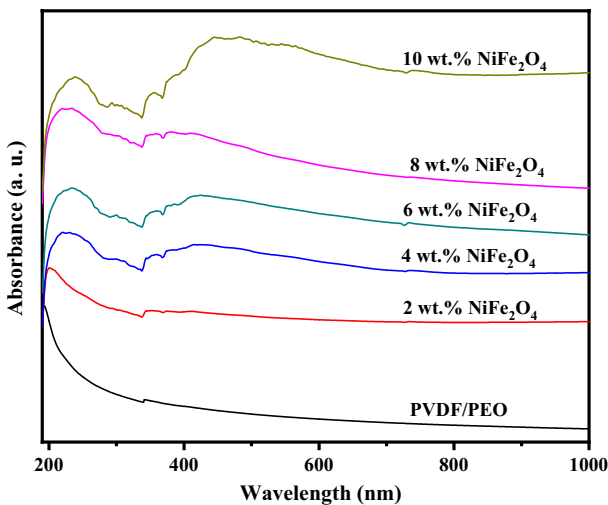


Fig. 7 UV–Vis spectra of (85/15 wt/wt%) PVDF/PEO and PVDF/PEO incorporated with (2, 4, 6, 8, 10 wt%) NiFe₂O₄ NPs

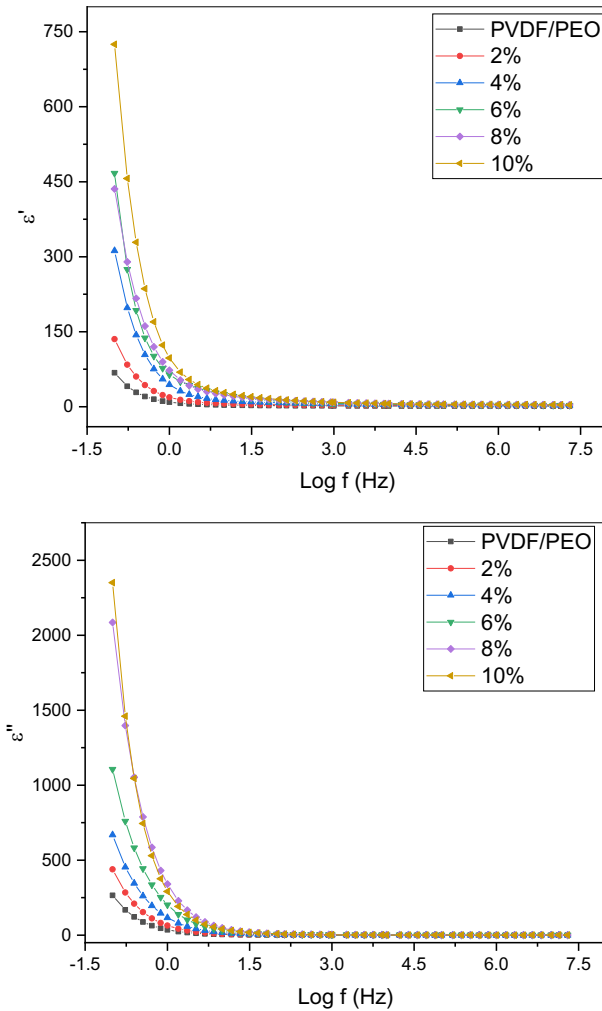


Fig. 8 The variation between ϵ' and ϵ'' with Log (f) for PVDF/PEO blend doped by 0, 2, 4, 6, 8 and 10 wt% of Nickel ferrite (NiFe_2O_4)

dielectric constant drops. At very high frequencies, dipoles can no longer follow the field and hence the dielectric constant reaches its minimum value. The value of ϵ' is increased from 68 to 726 while the ϵ'' value is increased from 261 to 2364 as an increase [41] of NiFe_2O_4 due to the high value of dielectric permittivity of NiFe_2O_4 as a filler and related to the interaction between NiFe_2O_4 with functionally groups in PVDF/PEO and the changing of the dipole arrangement gives variation in the dielectric properties. The dispersions of ϵ' and ϵ'' spectra may arise from the electronic and ionic dipole at the highest values of the frequency and due to polarization at the surface in the samples at the lower frequency. At low frequencies, we see that the values of the dielectric constant (ϵ') are at their

maximum due to the effect of moving ions that cause higher ionic conductivity [42, 43].

The complex modulus formula is a very important and convenient measurement tool for identifying, analyzing, and interpreting the dynamic aspects of the electrical transport process in a material. The electric modulus (M^*) is useful in rationalizing the conduction mechanisms and identifying the microscopic processes responsible for the local dielectric relaxation and polarization processes. The modulus (M^*) is defined as reciprocal dielectric permittivity (ϵ^*) [29–32]:

$$M^* = \frac{1}{\epsilon^*} = M' + M'' = \frac{\epsilon'}{\epsilon'^2 + \epsilon''^2} + \frac{\epsilon''}{\epsilon'^2 + \epsilon''^2} \quad (8)$$

where M' is the real part and M'' is the imaginary part for the electric modulus.

Figure 9a, b depicts the relation between both M' and M'' with $\text{Log}(f)$ for the present system. The real part (M') values about minimum values at the lower frequencies due to the negligible contribution of electrode polarization indicate that the electrode effect has a marginal electrode polarization. Further, the minimum values of the capacitive nature of the polymeric material are found at low frequency. Then, an increase of M' to reach the plateau at the intermediate region of the frequency and a linear increase at high frequencies. As we see in Fig. 9b, the appearance of semi-circles or arc in the spectrum of the relation between M'' with $\text{Log}(f)$ confirms the single phase of the materials.

Figure 10 depicts the graph between M' as a function and $\text{Log}(f)$ of the frequency of the PVDF/PEO with 10% wt of NiFe_2O_4 in the range of temperatures from 30 to 120 °C. At the lower frequency range, the values of M' are nearly zero because the restoring force gives the mobility of charge carriers. This suggests the long-range mobility of charge carriers due to electrode polarization. Also, an increase of M' with increasing frequency has been founded, supporting the conduction phenomena. At the higher range of the frequency, the values of M' reach the maximum value. This behavior of M' is inversely proportional to ϵ' . At higher temperatures, M' levels off at frequencies higher than those at lower temperatures because the relaxation processes are spread over a range of frequencies.

Figure 11 depicts the graph between the imaginary part of (M'') and $\text{Log}(f)$ of the frequency of the prepared samples. As we have seen, the given spectrum is asymmetric concerning the maximum peak. We saw broadening at each peak on either side of the peak maximum indicated by Debye's exemplary behavior. It was interpreted depending on the relaxation time distributions attributed to the nature of the material other than Debye, and the charge carriers appeared traveling in the range over long distances with low frequencies located to the left of the peaks. While in the area to the right of the peak, the peak area indicates the transition from long-range to short-term mobility. The extreme shifts of the spectral modulus M'' toward higher frequencies with an increasing indication that the dielectric relaxation is thermally activated also.

In general, the measurement of $\tan \delta$ as a function of frequency often a loss is attributed to polarization and conduction inside the composite samples [44]. Figure 12 depicts the variation dissipation loss factor ($\tan \delta$) as a function of frequency

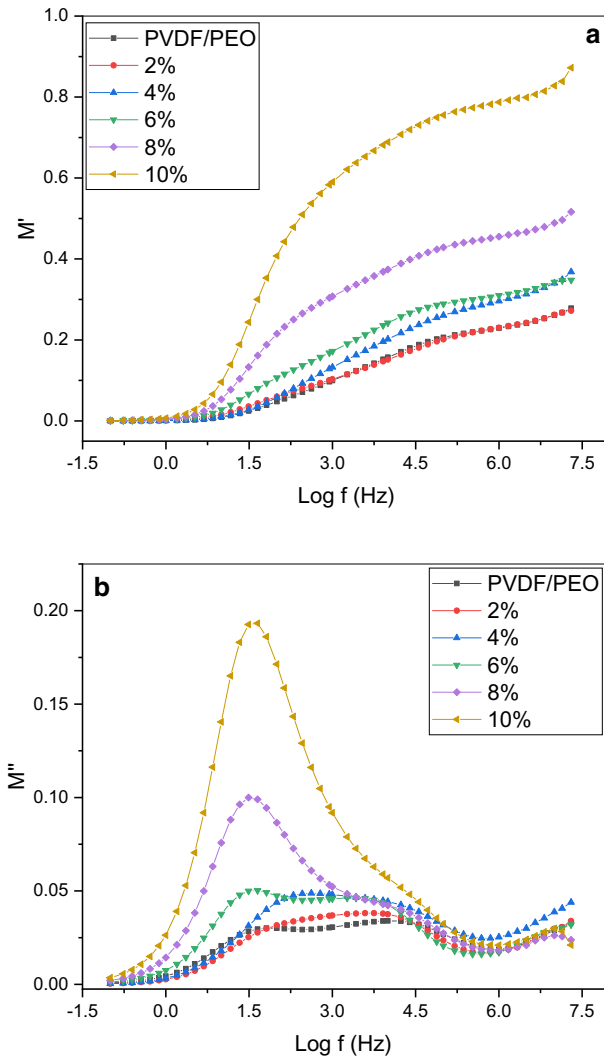


Fig. 9 The relation between both M' and M'' with $\text{Log } (f)$ for PVDF/PEO blend doped by 0, 2, 4, 6, 8 and 10 wt% of Nickel ferrite (NiFe_2O_4)

at different temperatures. The $\tan \delta$ values increase with the frequency values, pass through a maximum value of $\tan \delta$, and then decrease. The maximum values of $\tan \delta$, which get shifted to the higher frequency, confirm that the samples can be represented by a parallel combination of resistance (R) and capacitance (C). The highest value (peak) found at intermediate of the frequency confirms the relaxation phenomenon. The minimum values of tangent loss ($\tan \delta$) for the pure polymer blend may be due to the amorphous nature, which increased after the addition of NiFe_2O_4 due to an increase in the crystallinity.

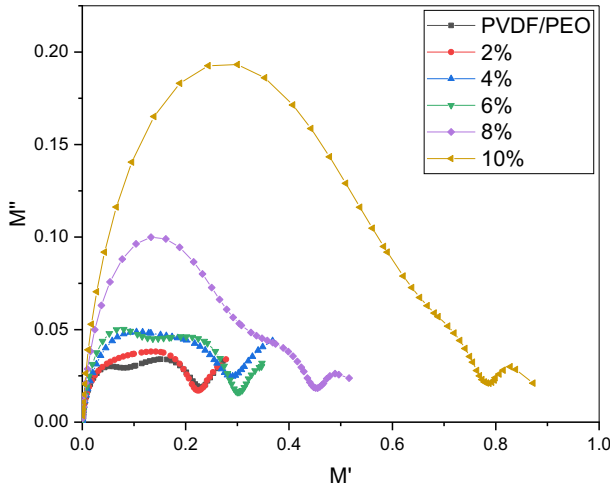


Fig. 10 The graph between M'' as a function and $\text{Log}(f)$ of the frequency the PVDF/PEO with 10% wt of NiFe_2O_4 in the range of temperatures from 30 to 120 °C

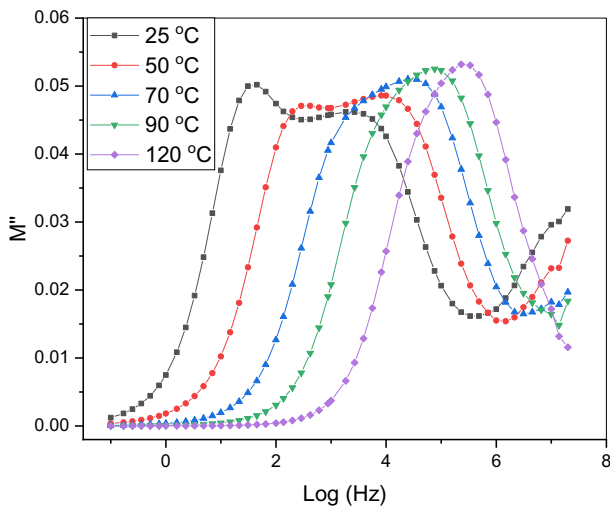


Fig. 11 The graph between the imaginary part of (M'') and Log (of the frequency) the PVDF/PEO with 10% wt of NiFe_2O_4 in the range of temperatures from 30 to 120 °C

Magnetization data allow determining the magnetic parameters such as saturation magnetization (M_s), saturation retentively or remanence magnetization (M_r), and coercive force (H_{ci}), where H_{ci} is the field needed to bring the magnetization back to zero. Figure 13 shows the magnetization (emu/g) as a function of magnetic field (Oe) of pure nickel ferrite (NiFe_2O_4) nanoparticles in the range from -20 to $+20$ kOe. The magnetization parameters for pure NiFe_2O_4 are measured

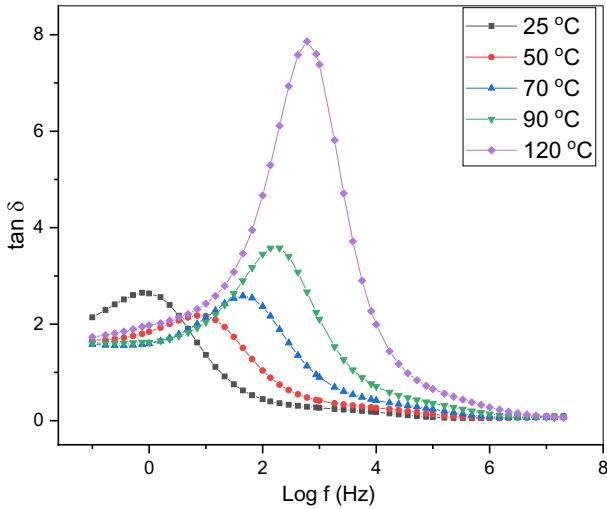


Fig. 12 The variation dissipation loss factor ($\tan \delta$) as a function of frequency at different temperatures

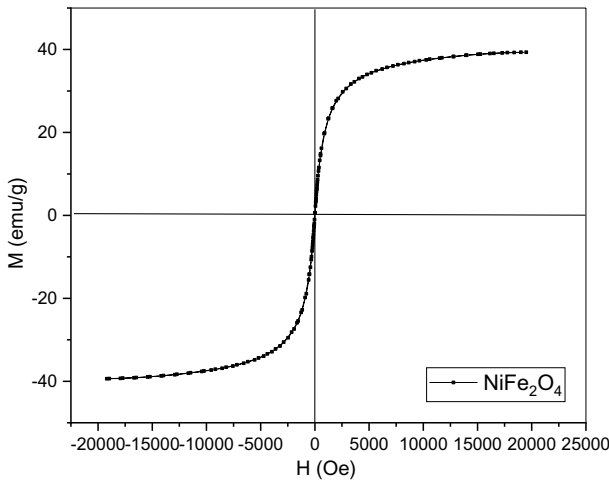


Fig. 13 The magnetization (emu/g) as a function of magnetic field (Oe) of pure Nickel Ferrite (NiFe_2O_4) nanoparticles in the range from -20 to $+20$ kOe

to be $M_s = 39.38$ emu/g, $M_r = 8.3 \times 10^{-2}$ emu/g and $H_{ci} = 2.28$ G. The saturation magnetization values exhibit a paramagnetic behavior of pure NiFe_2O_4 .

Figure 14 shows the magnetization against the magnetic field of PVDF/PEO blend doped with 0, 0.4, 0.8 and 1.2 wt% of NiFe_2O_4 nanoparticles. As expected for the polymeric materials, the magnetization of the PVDF/PEO blend is close to zero due to the absence of NiFe_2O_4 nanoparticles embedded in nonmagnetic blend matrices.

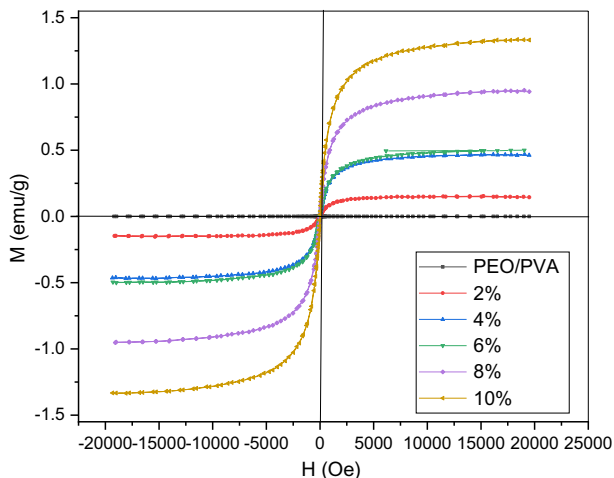


Fig. 14 The magnetization against the magnetic field of PVDF/PEO blend doped with 0, 0.4, 0.8 and 1.2 wt% of NiFe₂O₄ nanoparticles

The values of saturation magnetization of PVDF/PEO incorporated by NiFe₂O₄ is increased linearly as an increase of NiFe₂O₄ content as the following: ≈ 0.15 emu/g for the sample 2% of NiFe₂O₄-PVDF/PEO; 0.46 emu/g for the sample 4% of NiFe₂O₄-PVDF/PEO; 0.499 emu/g for the sample 6% of NiFe₂O₄-PVDF/PEO; 0.95 emu/g for the sample 8% of NiFe₂O₄-PVDF/PEO and 1.34 emu/g for the sample 10% of NiFe₂O₄-PVDF/PEO. This indicates an improved magnetic vector arrangement because NiFe₂O₄ nanoparticles are embedded into a nonmagnetic polymer matrix. The magnetic nanoparticles are concentrated into a chain-like shape due to the magnetic induction, thus enhancing magnetic interactions between dipole and dipole particles. Structure, the projection of the magnetization vector along the direction of the field will be higher than the random projection distribution of NiFe₂O₄ nanoparticles in the PVDF/PEO matrix with a large-shaped contrast effect.

The results indicate that the magnetic behavior observed in the nanocomposites originated from the magnetic NiFe₂O₄ nanoparticles attributed to the increasing tendency of the nanoparticles to aggregate on increasing their content. Whereby arise increase in the NiFe₂O₄ content increases the magnetic moment per unit volume of the prepared sample, which leads to a rising increase in its magnetization. It was also certain that the M_s values of the composites were much lower than the values of the bulk magnetic particles. The magnetic values of the compounds indicate a magnetic behavior caused by the addition of NiFe₂O₄. The magnetization parameters of NiFe₂O₄-PVDF/PEO to be M_s , M_r and H_{ci} are tabulated in Table 2. Due to the magnetic properties of the samples, they can further exploit the magnetic composite films for magnetic applications.

Table 2 Values of M_s , M_r and H_{ci} NiFe₂O₄-PVDF/PEO nanocomposites

| NiFe ₂ O ₄ wt% | M_s emu/g | M_r emu/g | H_{ci} G |
|---|----------------|-----------------------|---------------|
| 0 | 0.0 | 0.0 | 0.0 |
| 2 | 0.15 | 6.1×10^{-4} | 3.96 |
| 4 | 0.46 | 1.5×10^{-3} | 2.26 |
| 6 | 0.49 | 8.4×10^{-4} | 0.75 |
| 8 | 1.34 | 1.97×10^{-3} | 3.49 |
| 10 | 39.38 | 6.1×10^{-3} | 1.87 |

Conclusions

Pure nickel ferrite (NiFe₂O₄) nanoparticles were prepared by the solvothermal method and characterized using XRD, TEM, FESEM, and ATR-FTIR techniques. Different concentrations NiFe₂O₄NPs were added to PVDF/PEO using the casting technique. The XRD, TEM, and FESEM measurements show that NiFe₂O₄ NPs have a semispherical shape and round edges. The nanocomposites have a polycrystalline structure with 4.3–8.8 nm particle size. The data confirmed the interaction between PVDF/PEO and the NiFe₂O₄ NPs. NiFe₂O₄ NPs image shows that micro-metrical agglomeration suggests the presence of free crystallites on the surface. The 3D image reveals that the surface of PVDF/PEO becomes rougher means that the PVDF/PEO-NiFe₂O₄were improved to be suitable for industrial application. The dielectric constant (ϵ') was dramatically decreased with an increase in frequency. The dielectric constant and dielectric loss were enhanced after the addition of NiFe₂O₄ due to the effect of moving ions that cause higher ionic conductivity. The appearance of semi-circles in the plot of M'' with Log f confirms the single phase of the samples. The dielectric trend shows that M' was inversely proportional to ϵ' . The saturation magnetization values have been linearly increased as an increase of NiFe₂O₄ indicates an improvement in the magnetic vector arrangement. Due to the magnetic properties, they can further exploit the films for magnetic applications.

Funding Open access funding provided by The Science, Technology & Innovation Funding Authority (STDF) in cooperation with The Egyptian Knowledge Bank (EKB).

Declarations

Conflict of interest The authors declare that they have no conflict of interest.

Open Access This article is licensed under a Creative Commons Attribution 4.0 International License, which permits use, sharing, adaptation, distribution and reproduction in any medium or format, as long as you give appropriate credit to the original author(s) and the source, provide a link to the Creative Commons licence, and indicate if changes were made. The images or other third party material in this article are included in the article’s Creative Commons licence, unless indicated otherwise in a credit line to the material. If material is not included in the article’s Creative Commons licence and your intended use is not permitted by statutory regulation or exceeds the permitted use, you will need to obtain permission

directly from the copyright holder. To view a copy of this licence, visit <http://creativecommons.org/licenses/by/4.0/>.

References

1. El-Denglawey A, Angadi VJ, Manjunatha K, Chethan B, Somvanshi SB (2021) Role of dysprosium in enhancing the humidity sensing performance in manganese zinc ferrites for sensor applications. *J Mater Sci Mater Electron* 32:23554–23565. <https://doi.org/10.1007/s10854-021-06842-1>
2. Borade RM, Somvanshi SB, Kale SB, Pawar RP, Jadhav KM (2020) Spinel zinc ferrite nanoparticles: an active nanocatalyst for microwave irradiated solvent free synthesis of chalcones. *Mater Res Express*. <https://doi.org/10.1088/2053-1591/ab6c9c>
3. Andhare DD, Jadhav SA, Khedkar MV, Somvanshi SB, More SD, Jadhav KM (2020) Structural and chemical properties of ZnFe₂O₄ nanoparticles synthesised by chemical co-precipitation technique. *J Phys Conf Ser*. <https://doi.org/10.1088/1742-6596/1644/1/012014>
4. Gulkesen S, Tumen KU, Akyol M, Ekicibil A (2021) Room-temperature magnetocaloric effect in Fe-substituted CoCr₂O₄ spinels. *Appl Phys A Mater Sci Process* 127:1–10. <https://doi.org/10.1007/s00339-021-04374-3>
5. Patade SR, Andhare DD, Somvanshi SB, Kharat PB, More SD, Jadhav KM (2020) Preparation and characterisations of magnetic nanofluid of zinc ferrite for hyperthermia. *Nanomater Energy* 9:8–13. <https://doi.org/10.1680/jnaen.19.00006>
6. Patade SR, Andhare DD, Somvanshi SB, Kharat PB, Jadhav KM (2020) Effect of zinc doping on water-based manganese ferrite nanofluids for magnetic hyperthermia application. *AIP Conf Proc*. <https://doi.org/10.1063/5.0017051>
7. Kharat PB, Somvanshi SB, Jadhav KM (2020) Multifunctional magnetic nano-platforms for advanced biomedical applications: a brief review. *J Phys Conf Ser*. <https://doi.org/10.1088/1742-6596/1644/1/012036>
8. Kharat PB, Somvanshi SB, Khirade PP, Jadhav KM (2020) Effect of magnetic field on thermal conductivity of the cobalt ferrite magnetic nanofluids. *J Phys Conf Ser*. <https://doi.org/10.1088/1742-6596/1644/1/012028>
9. Kharat PB, Somvanshi SB, Khirade PP, Jadhav KM (2020) Induction heating analysis of surface-functionalized nanoscale CoFe₂O₄ for magnetic fluid hyperthermia toward noninvasive cancer treatment. *ACS Omega* 5:23378–23384. <https://doi.org/10.1021/acsomega.0c03332>
10. Jadhav SA, Khedkar MV, Somvanshi SB, Jadhav KM (2021) Magnetically retrievable nanoscale nickel ferrites: an active photocatalyst for toxic dye removal applications. *Ceram Int* 47:28623–28633. <https://doi.org/10.1016/j.ceramint.2021.07.021>
11. Chavan AR, Khirade PP, Somvanshi SB, Mukhamale SV, Jadhav KM (2021) Eco-friendly green synthesis and characterizations of CoFe_{2-x}Al_xO₄ nanocrystals: analysis of structural, magnetic, electrical, and dielectric properties. *J Nanostruct Chem* 11:469–481. <https://doi.org/10.1007/s40097-020-00381-7>
12. Khan I, Saeed K, Khan I (2019) Nanoparticles: properties, applications and toxicities. *Arab J Chem* 12:908–931. <https://doi.org/10.1016/j.arabj.2017.05.011>
13. Jeevanandam J, Barhoum A, Chan YS, Dufresne A, Danquah MK (2018) Review on nanoparticles and nanostructured materials: history, sources, toxicity and regulations. *Beilstein J Nanotechnol* 9:1050–1074. <https://doi.org/10.3762/bjnano.9.98>
14. Nejati K, Zabihi R (2012) Preparation and magnetic properties of nano Mn-Zn ferrite particles. *Chem Cent* 43:37–41
15. Marinca TF, Chicinas I, Isnard O, Pop V, Popa F (2011) Synthesis, structural and magnetic characterization of nanocrystalline nickel ferrite—NiFe₂O₄ obtained by reactive milling. *J Alloys Compd* 509:7931–7936. <https://doi.org/10.1016/j.jallcom.2011.05.040>
16. Li P, Ma R, Zhou Y, Chen Y, Liu Q, Peng G, Liang Z, Wang J (2015) Spinel nickel ferrite nanoparticles strongly cross-linked with multiwalled carbon nanotubes as a bi-efficient electrocatalyst for oxygen reduction and oxygen evolution. *RSC Adv* 5:73834–73841. <https://doi.org/10.1039/c5ra14713a>

17. Li DY, Sun YK, Gao PZ, Zhang XL, Ge HL (2014) Structural and magnetic properties of nickel ferrite nanoparticles synthesized via a template-assisted sol-gel method. *Ceram Int* 40:16529–16534. <https://doi.org/10.1016/j.ceramint.2014.08.006>
18. Aliahmad M, Noori M, Kargan NH, Sargazi M (2013) Synthesis of nickel ferrite nanoparticles by co-precipitation chemical method. *Int J Phys Sci* 8:854–858. <https://doi.org/10.5897/ijps11.517>
19. Huang YR, Jiang Y, Hor JL, Gupta R, Zhang L, Stebe KJ, Feng G, Turner KT, Lee D (2015) Polymer nanocomposite films with extremely high nanoparticle loadings via capillary rise infiltration (CaRI). *Nanoscale* 7:798–805. <https://doi.org/10.1039/c4nr05464d>
20. Zhan C, Yu G, Lu Y, Wang L, Wujcik E, Wei S (2017) Conductive polymer nanocomposites: a critical review of modern advanced devices. *J Mater Chem C* 5:1569–1585. <https://doi.org/10.1039/c6tc04269d>
21. Rosyadah Ahmad NN, Mukhtar H, Mohshim DF, Nasir R, Man Z (2016) Surface modification in inorganic filler of mixed matrix membrane for enhancing the gas separation performance. *Rev Chem Eng* 32:181–200. <https://doi.org/10.1515/revce-2015-0031>
22. Sim LH, Gan SN, Chan CH, Kammer HW, Yahya R (2009) Compatibility and conductivity of LiClO₄ free and doped polyacrylate–poly (ethylene oxide) blends. *Mater Res Innov* 13:278–281. <https://doi.org/10.1179/143307509X440523>
23. Stephan AM (2006) Review on gel polymer electrolytes for lithium batteries. *Eur Polym J* 42:21–42. <https://doi.org/10.1016/j.eurpolymj.2005.09.017>
24. Nawawi MA, Har SL, Han CC (2012) Miscibility of polymer blends comprising poly (ethylene oxide)-epoxidized natural rubber. *Int J Chem Eng Appl*. <https://doi.org/10.7763/ijcea.2012.v3.230>
25. Alhusaiki-Alghamdi HM (2017) Thermal and electrical properties of graphene incorporated into polyvinylidene fluoride/polymethyl methacrylate nanocomposites. *Polym Compos* 38:E246–E253. <https://doi.org/10.1002/pc.23997>
26. Patterson AL (1939) The scherrer formula for X-ray particle size determination. *Phys Rev* 56:978–982. <https://doi.org/10.1103/PhysRev.56.978>
27. Somvanshi SB, Khedkar MV, Kharat PB, Jadhav KM (2019) Influential diamagnetic magnesium (Mg²⁺) ion substitution in nano-spinel zinc ferrite (ZnFe₂O₄): thermal, structural, spectral, optical and physisorption analysis. *Ceram Int*. <https://doi.org/10.1016/j.ceramint.2019.12.097>
28. Somvanshi SB, Jadhav SA, Khedkar MV, Kharat PB, More SD, Jadhav KM (2020) Structural, thermal, spectral, optical and surface analysis of rare earth metal ion (Gd³⁺) doped mixed Zn–Mg nano-spinel ferrites. *Ceram Int*. <https://doi.org/10.1016/j.ceramint.2020.02.091>
29. Jadhav KM (2020) Cation distribution, magnetic and hyperfine interaction studies of Ni–Zn spinel ferrites: role of Jahn teller ion (Cu²⁺) substitution. *Mater Adv*. <https://doi.org/10.1039/d0ma00251h>
30. Zhu S, Ni J, Feng S (2019) Investigation on magnetic power loss in strontium doped Ba_{1-x}Sr_xTi₁₋₂Co₁₋₂Fe_{9.6}O₁₉ hexaferrites. *Mater Res Express* 6:116102
31. Bhosale AB, Somvanshi SB, Murumkar VD, Jadhav KM (2020) Influential incorporation of RE metal ion (Dy³⁺) in yttrium iron garnet (YIG) nanoparticles: magnetic, electrical and dielectric behaviour. *Ceram Int* 46:15372–15378. <https://doi.org/10.1016/j.ceramint.2020.03.081>
32. Hafez RS, Hakeem NA, Ward AA, Ismail AM, El-kader FHA (2020) Dielectric and thermal properties of PEO/PVDF blend doped with different concentrations of Li₄Ti₅O₁₂ nanoparticles. *J Inorg Organomet Polym Mater* 30:4468–4480. <https://doi.org/10.1007/s10904-020-01637-z>
33. Ali H, Ismail AM (2021) Developing montmorillonite/PVDF/PEO microporous membranes for removal of malachite green: adsorption, isotherms, and kinetics. *J Polym Res*. <https://doi.org/10.1007/s10965-021-02789-3>
34. Chen P, Liang X, Wang J, Zhang D, Yang S, Wu W, Zhang W, Fan X, Zhang D (2017) PEO/PVDF-based gel polymer electrolyte by incorporating nano-TiO₂ for electrochromic glass. *J Sol Gel Sci Technol* 81:850–858. <https://doi.org/10.1007/s10971-016-4235-5>
35. Grujić A, Čosović V, Stajčić-Trošić J, Čosović A, Stjepović M, Putić L, Žák T (2018) Synthesis of NiFe₂O₄ nanofibers by joint sol–gel and electrospinning technique. *Metall Mater Eng* 24:173–180. <https://doi.org/10.30544/387>
36. Dhatarwal P, Sengwa RJ (2020) Synergistic effects of salt concentration and polymer blend composition on the crystal phases, dielectric relaxation, and ion conduction in PVDF/PEO/LiCF₃SO₃ solid polymer electrolytes. *Ionics (Kiel)* 26:2259–2275. <https://doi.org/10.1007/s11581-019-03337-2>
37. Pradeepa P, Edwin Raj S, Sowmya G, Kalaiselvarmy J, Ramesh Prabhu M (2016) Optimization of hybrid polymer electrolytes with the effect of lithium salt concentration in PEO/PVdF-HFP blends.

- Mater Sci Eng B Solid State Mater Adv Technol 205:6–17. <https://doi.org/10.1016/j.mseb.2015.11.009>
38. Taj MB, Alkahtani MDF, Raheel A, Shabbir S, Fatima R, Aroob S, Yahya R, Alelwani W, Alahmadi N, Abualnaja M, Noor S, Ahmad RH, Alshater H (2021) Bioconjugate synthesis, phytochemical analysis, and optical activity of NiFe_2O_4 nanoparticles for the removal of ciprofloxacin and congo red from water. *Sci Rep* 11:1–19. <https://doi.org/10.1038/s41598-021-84983-3>
 39. Gökçen M, Tunç T (2013) Enhancement of dielectric characteristics of polyvinyl alcohol (PVA) interfacial layer in Au/PVA/n-Si structures by Bi_2O_3 disperse. *Int J Appl Ceram Technol* 10:E64–E69. <https://doi.org/10.1111/ijac.12009>
 40. Prabu M, Selvasekarapandian S (2012) Dielectric and modulus studies of LiNiPO_4 . *Mater Chem Phys* 134:366–370. <https://doi.org/10.1016/j.matchemphys.2012.03.003>
 41. Kumar KN, Misook KS, Ratnakaram KYC (2016) Improved electrical properties of Fe nanofiller impregnated PEO + PVP: Li^+ blended polymer electrolytes for lithium battery applications. *Appl Phys A*. <https://doi.org/10.1007/s00339-016-0212-7>
 42. Saijyothi KNKK (2017) Copper–constantan nanoparticles impregnated PEO + PVP: Li^+ blended solid polymer electrolyte films for lithium battery applications. *Polym Bull* 74:2545–2564. <https://doi.org/10.1007/s00289-016-1849-2>
 43. Kumar KN, Kang M, Sivaiah K, Ravi M, Ratnakaram YC (2016) Enhanced electrical properties of polyethylene oxide (PEO)+ polyvinylpyrrolidone (PVP): Li^+ blended polymer electrolyte films with addition of Ag nanofiller. *Ionics (Kiel)*. <https://doi.org/10.1007/s11581-015-1599-4>
 44. Lahlali S, Essaleh L, Belaqqiz M, Chehouani H, Alimoussa A, Djessas K, Viallet B, Gauffier JL, Cayez S (2017) Dielectric and modulus analysis of the photoabsorber Cu_2SnS_3 . *Phys B Condens Matter* 526:54–58. <https://doi.org/10.1016/j.physb.2017.09.069>

Publisher's Note Springer Nature remains neutral with regard to jurisdictional claims in published maps and institutional affiliations.